PAPER

Hydrodynamic Considerations in Near-Optimal Control of a Small Wave Energy Converter for Ocean Measurement Applications

AUTHORS

Umesh A. Korde
Jiajun Song
Rush D. Robinett III
Ossama O. Abdelkhalik
Department of Mechanical Engineering-Engineering Mechanics, Michigan Technological University

ABSTRACT

This paper investigates the use of wave energy to power long-term ocean sensing systems. The device examined here consists of an oceanographic buoy and a shallow-submerged reaction frame that may carry a science instrument. Power conversion is from the relative heave oscillation between the two bodies. The oscillation is controlled on a wave-by-wave basis using near-optimal feedforward control, which requires up-wave surface elevation measurement and deterministic prediction at the device location. This paper presents the dynamic formulation used to evaluate the near-optimal, wave-by-wave control forces in the time domain. Also examined are reaction-frame geometries for their impact on overall power capture through favorable hydrodynamic interactions. Performance is evaluated in a range of wave conditions (from most to least favorable for conversion) sampled over a year at a chosen site of deployment. It is found that control may be able to provide the required amounts of power to sustain instrument operation at the chosen site but also that energy storage options may be worth pursuing.

Keywords: ocean sensing, wave energy, small converters, efficient conversion, wave-by-wave control

Background and Introduction

Many wave energy devices convert power using the relative oscillation of floating bodies with respect to a reference body that is stationary or nearly stationary (Falcao, 2010). Typically,

Nomenclature

α_r	Maximum displacement allowed by the swept volume constraint
$\beta_r(\omega)$	Velocity constraint
$\eta(x; i\omega)$	Frequency-domain expression for wave surface elevation
$\eta(x, t)$	Time-domain wave surface elevation at point x and time t
ω	Angular frequency of wave/oscillation
$\bar{a}_t(\omega)$, $\bar{a}_b(\omega)$	Added mass variations for the top and bottom bodies, respectively, inclusive of infinite-frequency parts
A	Incident wave amplitude
$a_c(\omega)$, $b_c(\omega)$	Added mass and radiation damping coefficients representing the frequency-dependent radiation coupling between the top and bottom bodies
$b_t(\omega)$, $b_b(\omega)$	Radiation damping variations for the top and bottom bodies, respectively
c_{dt}, c_{db}	Linearized, constant viscous damping coefficients for the top and bottom bodies, respectively
D	Constant damping load applied on the relative heave oscillation
d	Distance between the up-wave measurement point and the device centroid; $x_B - x_A$
$F_a(t)$	Reactive control force applied by the power takeoff
$F_e(i\omega)$	Effective heave force
$F_l(t)$	Resistive control force applied by the power takeoff
$F_{fb}(i\omega)$	Exciting force coefficient of reaction frame
F_{ft}, F_{fb}	Exciting forces on the top and bottom bodies, respectively
$F_{ft}(i\omega)$	Exciting force coefficient of standard buoy

$F_{\text{relative}}(i\omega)$	Relative exciting force coefficient
$F_{\text{total}}(i\omega)$	Total exciting force coefficient
g	Acceleration of gravity
$h_{\text{l}}(t; d)$	Impulse response function defining the deterministic propagation model for distance d
$H_{\text{s1(2)}}$	Significant wave height for swell (wind) seas
$k(\omega)$	Wave number; related to angular frequency ω through the dispersion relation
k_{t}, k_{b}	Stiffness constants determining the restoring forces on the top and bottom bodies, respectively
m_{t}, m_{b}	In-air masses of the top and bottom bodies, respectively
P_{ω}	Average power absorbed over time T
R_{i}	Relative radiation damping coefficient
$R_{\text{i}}(\omega)$, $C_{\text{i}}(\omega)$	Equivalent hydrodynamic damping and reactance components "acting on" the relative oscillation between the two bodies
s	Geometric scale factor, defined as ratio of full-scale length dimension and model-scale length dimension
$T_{\text{e1(2)}}$	Energy period for swell (wind) seas
v_{r}, x_{r}	Relative heave velocity and displacement between the top and bottom bodies
v_{t}, v_{b}	Heave oscillation velocities of the top and bottom bodies, respectively
$v_{\text{ro}}(i\omega)$	Hydrodynamically optimum velocity
Z_{b}	Complex impedance of the bottom body
Z_{c}	Complex impedance representing radiation coupling between the top and bottom bodies
Z_{L}	Complex impedance representing resistive and reactive loads
Z_{t}	Complex impedance of the top body

the floating bodies are designed so that their natural periods approximately match a chosen range of energy periods in the wave scatter diagram for a deployment site. As wave conditions change over seasons, power conversion performance drops. Wave energy devices thus often tend to be bulky and uneconomical in terms of annual power generation and overall costs. Smaller devices are of interest because they experience smaller structural loads (Count, 1978) and thus require smaller investments. Based on the practice of Froude scaling, power scales as $s^{3.5}$ with buoy radius, while wave period scales as $s^{0.5}$ (see, e.g., McCormick, 2010; Newman, 1978). Thus, for a given set of wave periods as determined by a given site of deployment, converted power scales as s^3. For this reason, smaller devices also convert considerably smaller power amounts in the same wave climates. Furthermore, most small devices have narrow response bandwidths, which make them highly sensitive to wave periods. However, they can be made more cost-effective if their dynamic response can be actively controlled to match incoming wave conditions. Such control was first attempted by Salter for the Edinburgh duck and Budal for a heaving buoy (Budal & Falnes, 1977; Salter, 1978). Recent years have seen a large number of control applications, as reviewed in Falcao (2010) and Ringwood et al. (2014). Control can involve a combination of reactive and resistive loading (applied by the power takeoff) (e.g., Hansen & Kramer, 2011; Korde, 2015a; Nebel, 1992) or resistive loading alone together with switching control of the device oscillation (e.g., Babarit & Clement, 2006; Budal & Falnes, 1980; Hoskin et al., 1985). The former approach is referred to as complex conjugate control for impedance matching, while the latter is termed "latching" when used to slow down the response of a small buoy to bring about force-velocity phase match in longer waves.

The few control approaches that have been attempted in practice have shown twofold to threefold improvements in energy capture (Hansen & Kramer, 2011) through the addition of reactive tuning to the baseline approaches based on resistive loading alone. Further improvements require wave-by-wave control, which is difficult to apply because wave-by-wave reactive cancellation and resistive match (i.e., wave-by-wave impedance matching) require knowledge of the future oscillations/wave elevations (Falnes, 1995; Naito & Nakamura, 1985). Operation close to optimum velocity frequently results in excessive velocities and very large displacements. Practical limitations require oscillation constraints. An intuitively natural constraint is based on the device swept volume, which limits the oscillation amplitude to buoy draft (or freeboard if smaller) (Falnes & Hals, 2012; Hals,

2013). Operation under oscillation constraints limits power conversion, especially for small buoys.

While much of the work referred to above was intended for ultimate application in large-scale energy generation, the focus of this work is on utilization of wave energy for power delivery to ocean-based measurements and monitoring operations. Thus, the goal of this paper is to investigate the energy conversion performance of a small buoy designed to be part of an oceanographic surface mooring system, which may limit the buoy size to about 1–1.2 m in radius and about 1-m draft. In addition, power conversion is designed to be via the relative oscillation between the floating buoy and a shallow-submerged axisymmetric reaction body that serves as an instrument frame (see Figure 1). Both the buoy and the instrument frame are excited by waves. The goal of this study is to evaluate wave-by-wave near-optimal control of the constrained relative oscillation between the buoy and the submerged body. In this paper, it is assumed that heave oscillations dominate, although for some of the geometries studied here, pitch moments may become significant (see Figure 2). The present work ignores this effect, although the authors recognize that it needs to be examined further. Power conversion is via a hydraulic actuator, which provides the forcing required for control and power conversion. The hydraulic system also includes an accumulator and control valves and uses biodegradable hydraulic fluid. The accumulator is designed to provide "short-term" energy storage on the time scale required for wave-by-wave control. Several idealizations are implicit in this study, and in particular, potential practical problems such as corrosion, fouling, and misalignments in hardware are neglected. Moreover, the present formulation is based on linear theory. The focus of this paper is on the control and design aspects of the two-body converter. Up-wave measurements and surface elevation predictions based on up-wave measurements are used for real-time evaluation of the actuator force (reactive + resistive) to be applied on a wave-by-wave basis. This force represents the feedforward force required to drive the relative heave oscillation velocity to the hydrodynamically optimum constrained velocity at which power conversion is maximized subject to the constraint.

Because the submerged body is close to the water surface and because both bodies are small compared with most wave lengths of interest, one expects that, in longer waves, the two bodies experience large in-phase oscillations. However, one of the goals of this paper is to investigate geometries that maximize the "force compensation" effect studied by Budal (1985) three decades ago (see also Falnes, 1998). Because the heave exciting forces on the two bodies depend on their geometries and on whether or not they are floating or submerged, it is worth investigating whether their geometries (and submergence, as in the case of the submerged body) can be designed to maximize the vertical force causing their relative heave oscillation, and minimize the vertical force causing a coupled heave oscillation (where the two bodies oscillate as if they were rigidly connected). Force compensation refers to a situation where the exciting force on the reaction body is acting downward (upward) when the exciting

FIGURE 1

Buoy (same size as the OOI Pioneer Array central surface mooring [Ocean Observatories Initiative, 2017; OOI Pioneer Array, 2017]) and a notional instrument frame housing a science instrument set. The buoy and instrument frame are both assumed to be slack moored in the present work. Only the relative heave oscillation is used here for conversion.

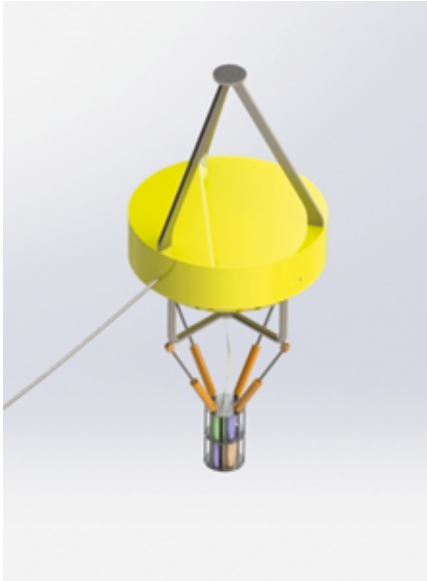

FIGURE 2

The heaving axisymmetric two-body device used in this work. Relative oscillation is used for energy conversion using a linear generator or hydraulic cylinder-type power takeoff mechanism/actuator, which is assumed to be linear and ideal (i.e., lossless). The figure shows the "starting/baseline" geometry for the submerged instrument frame composed of two circular discs held together by a central strut (not shown). The power takeoff also applies the required control force in this work, although in practice, it may be advantageous to use two actuators, one for power takeoff and one for reactive forcing.

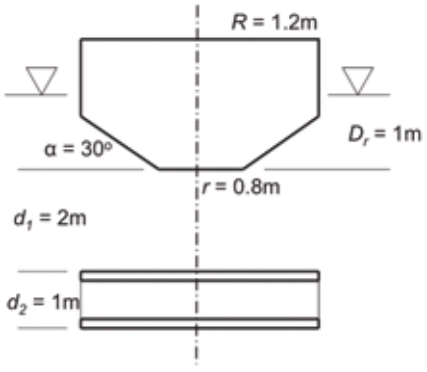

force on the device is acting upward (downward), enhancing their relative heave oscillation and decreasing coupled heave.[1] Note that it is only the relative oscillation between the bodies that is here utilized for energy conversion. Because, in this work, the goal is to integrate a wave energy converter into a commonly used oceanographic buoy design, the instrument frame geometry is the only "degree of freedom" available here for optimization of the force compensation effect. In addition, because good wave radiation implies good energy conversion (Evans et al., 1979; Falnes & Kurniawan, 2015), an effort is also made to maximize the effective radiation damping associated with the relative heave oscillation for the buoy-submerged body axisymmetric system. Although a number of geometries were examined in this paper, the most favorable three are selected for further evaluation through detailed power conversion simulations.

As mentioned, this paper utilizes wave predictions based on up-wave incident wave measurements to compute the feedforward actuation force required for approaching the hydrodynamically optimal relative heave oscillation. Performance of the system is tested through simulations in a range of wave climates. Wave statistics for this purpose are obtained from the site of a deployment for the instrument that forms the target application for the present design. The Deterministic Wave Prediction section after this introduction briefly summarizes the wave prediction approach used here. The Geometry Optimization section discusses the present approach to geometry optimization based on force compensation and effective radiation damping maximization. The Dynamic Model section outlines the dynamic model for the buoy-submerged body system and evaluates the feedforward control force. The calculations carried out here are summarized in the Calculations section. Principal results are discussed in the Discussion section. The paper ends with a brief section stating the main conclusions from this study.

[1]Recall that, in this work, the instrument frame serves as the reaction body, with the floating buoy being the device.

Deterministic Wave Prediction

The approach used here is based on the formulation described in Belmont et al. (2006) and Falnes (1995) and developed further in Korde (2015a). Here, the dynamics of wind-wave interactions over the free surface are ignored over the distance and time scales of interest. Hence, a linear kinematic model relating the wave surface elevation $\eta(x, t)$ at one point (time) to the wave surface elevation at another point and another time may be sufficient. However, Fourier transformability requires that the wave elevation $\eta(x, t) \rightarrow 0$ as $t \rightarrow \pm\infty$ (Newman, 1978; Schetzen, 1980). In practice, this limits application of the present approach to periods of wave activity between periods when the sea is relatively calm. In Korde (2015a), the distance separating the point of measurement x_A and the point of prediction x_B was on the order of 1,000 m, and an advancing time series of surface elevation spanning about 260 s was used to predict the wave elevation at the device centroid about 30 s into the future. The prediction time was based on the heave radiation impulse response function for the device (particularly the time at which it could be truncated without serious loss of accuracy).

In deep water, for unidirectional wave propagation, a kinematic model relating the wave elevation at point x_A to that at point x_B in the frequency domain can be expressed as

$$\eta(x_B; i\omega) = e^{-ik(\omega)d}\,\eta(x_A; i\omega) \tag{1}$$

where $k(\omega)$ using the deep-water dispersion relation is

$$k(\omega) = \frac{|\omega|\omega}{g} \tag{2}$$

$k(\omega)$ has the same sign as ω (which in the inverse Fourier transformation of equation (4) below ranges from $-\infty$ to ∞ for a full description of the time-domain function $h_1(t; d)$ below). The wave elevation time history for predominantly unidirectional waves may be obtained by a nondirectional wave rider buoy. For most realistic surface wave spectra over which a wave energy device operates, ω may be expected to be within finite approximate limits ω_l and ω_h. Because surface waves are dispersive, an impulsive excitation of the wave surface propagates over a range of group velocities $[v_{gmn}, v_{gmx}]$, where, for deep water,

FIGURE 3

Space-time diagram for real ocean waves. This is used along with the required prediction time to determine the distance and duration of the up-wave measurement.

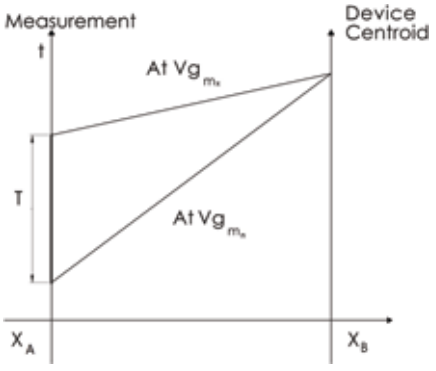

$$v_{gmn} = \frac{1}{2}\left(\frac{g}{\omega_{mx}}\right)$$
$$v_{gmx} = \frac{1}{2}\left(\frac{g}{\omega_{mn}}\right) \quad (3)$$

Figure 3 shows a space-time diagram relating the time series length, prediction time, prediction distance, and group velocity range considered. The prediction at x_B using a measurement at x_A can be obtained using an impulse response function $h_I(t; d)$, where

$$h_I(t; d) = \frac{1}{2\pi}\int_{-\infty}^{\infty} e^{-ik(\omega)d} e^{i\omega t} d\omega \quad (4)$$

$h_I(t; d)$ can be evaluated analytically as Falnes (1995), Belmont et al. (2006), and Korde (2015a) as

$$h_I(t; d) = \frac{1}{4}\sqrt{\frac{(2g)}{(\pi d)}}\left[\cos\frac{(gt^2)}{(4d)} + \sin\left(\frac{gt^2}{4d}\right)\right] + \frac{1}{2}\sqrt{\left(\frac{2g}{\pi d}\right)}\left[\cos\left(\frac{gt^2}{4d}\right) C\left(t\sqrt{\left(\frac{g}{2\pi d}\right)}\right)\right] + \frac{1}{2}\sqrt{\left(\frac{2g}{\pi d}\right)}\left[\sin\left(\frac{gt^2}{4d}\right) S\left(t\sqrt{\frac{g}{2\pi d}}\right)\right] \quad (5)$$

where C and S denote the two Fresnel integrals. Using a wave surface elevation time-series measurement at x_A over $[t - T, t]$ seconds, the surface elevation at $x_B = x_A + d$ at time $t + t_p$ can be obtained using

$$\eta(x_B;\ t + t_p) = \int_0^T T\, h_I(\tau)\eta(x_A;\ t - \tau)\, d\tau;\quad t > T$$
$$x_B - x_A = d = t_P\, v_{gmx}$$
$$T = \frac{d}{v_{gmn}} - \frac{d}{v_{gmx}} \quad (6)$$

Figure 4 shows a typical result for computer-generated irregular waves.

FIGURE 4

Comparison of computed wave elevation time domain history at x_B and predicted wave elevation history at x_f.

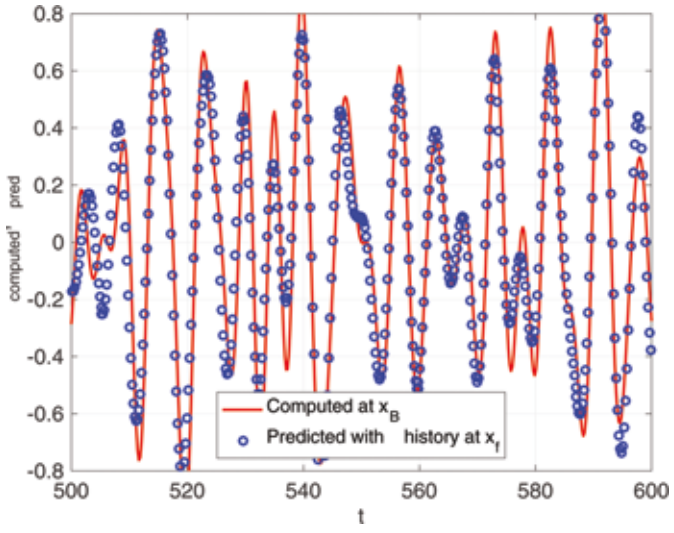

Geometry Optimization

Analysis software WAMIT (2012) is used to calculate the hydrodynamic coefficients of the proposed wave energy converter system in heave motion. Geometry input files of the floating buoy and reaction frame are defined separately to calculate the hydrodynamic interaction between the two bodies. The floating buoy is defined as shown in the upper part of Figure 2. The reaction frame is defined as two discs (spheres or hemispheres) connected with a rigid rod, as shown in the lower parts of Figures 5(a)–5(c). The design with two discs is taken to be the baseline geometry design. Although a number of geometries were examined, only the best three (in terms of the criteria below), including the baseline, are discussed here.

Preliminary evaluation is focused on total and relative exciting forces F_{total} and $F_{relative}$ as defined in equations (7) and (8). The first goal of geometry optimization is to maximize the relative exciting force and to minimize the total exciting force simultaneously, because high-energy capture ratio and small mooring force are results of high relative exciting force and low total exciting force. Results of exciting force evaluation for the three designs are shown in Figures 6(a)–6(c).

$$|F_{total}(i\omega)| = |F_{ft}(i\omega) + F_{fb}(i\omega)| \quad (7)$$

$$|F_{relative}(i\omega)| = |F_{ft}(i\omega) - F_{fb}(i\omega)| \quad (8)$$

Another evaluation is focused on relative radiation damping R_i, defined as the real part of the effective impedance (equation (15)) under no constraint. Note that the maximum energy captured is determined by the effective impedance on the relative heave motion of the system. One goal of geometry optimization is to maximize

FIGURE 5

Three of the different geometries tested as part of the work. (a) A standard oceanographic buoy with the original two-discs shape design of reaction frame; this figure shows input mesh file of WAMIT. A rigid connect is added between the two discs to help WAMIT recognize the two parts of WEC system: buoy and reaction frame. The radius of buoy and discs is 1.2 m, the thickness of discs is 0.1 m, and the equivalent draft of buoy is 1 m. Spacing between the bottom surface of buoy and the top surface of discs is 2 m. (b) Buoy with the original two-spheres shape design of reaction frame; this figure shows input mesh file of WAMIT. The radius of spheres is 1.2 m, the distance between buoy and top sphere is 2 m, and the distance between the two spheres is 1 m. (c) Buoy with the original two-hemispheres shape design of reaction frame; this figure shows input mesh file of WAMIT. The radius of hemispheres is 1.2 m, the distance between the top hemisphere and the buoy is 2 m, and the distance between the two hemispheres is 1 m.

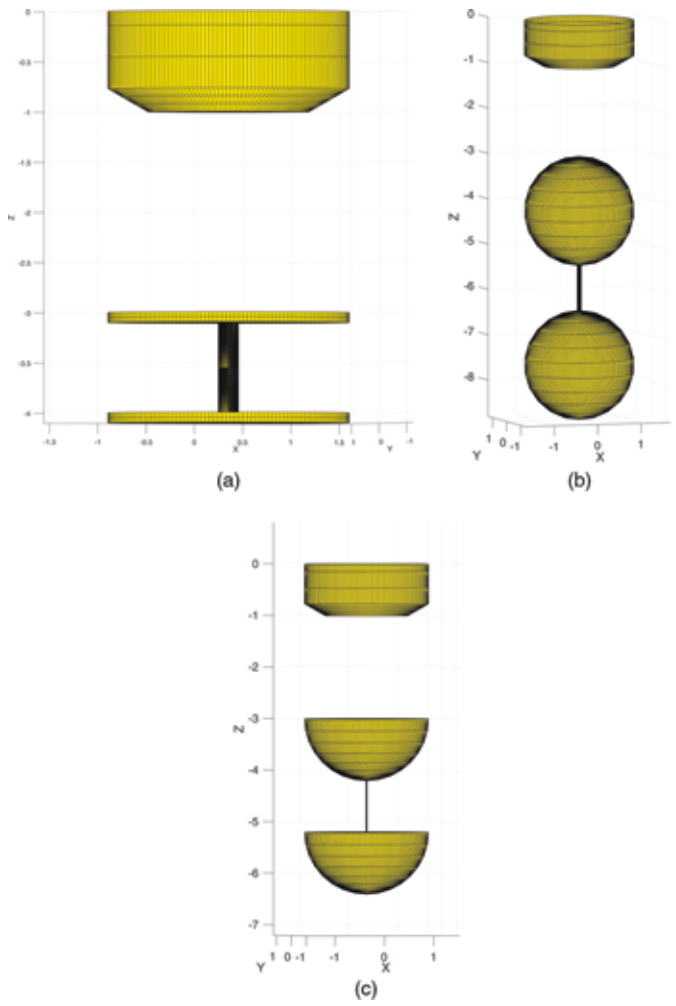

the peak value and the average value of the relative radiation damping simultaneously. A high peak value for the relative radiation damping results in high-energy capture ratio at a certain frequency of the incoming wave. High average values of the relative damping result in good energy capture over the whole incoming wave spectrum.

Cylindrical, spherical, and hemispherical shapes with different dimensions (e.g., radius) were evaluated. During geometry optimization, high weights were given to relative radiation damping, as R_i represents the resistive part of the power take-off (PTO) control force in heave motion without constraint. High peak values of relative radiation damping and high relative exciting force are found in shape designs with the same radius as the floating buoy. High values of R_i and $F_{relative}$ at low frequency are found concurrently in the spherical and hemispherical shape designs. As shown in Figures 7(a)–7(c), although the two-spheres design shows better relative exciting force over the frequency range of interest (Figure 6), the two-hemispheres design has the highest relative radiation damping coefficient at low frequencies and generally higher (compared with the other two geometries) relative radiation damping over the whole frequency range.

Energy capture simulations based on realistic yearlong wave data at Martha's Vineyard Coastal Observatory (MVCO, 2017) were performed on the three proposed designs above. The two-hemispheres design with higher relative radiation damping coefficient results in more energy capture under the same oscillation constraint conditions (Figures 8 and 9). The two-spheres design with higher relative exciting force results in less control force under the same oscillation constraint conditions (Figure 8(b)).

Dynamic Model

The approach below considers an axisymmetric omnidirectional wave energy converter based on relative heave oscillation of two bodies, although it should apply to other devices with appropriate modifications. Figure 2 shows the starting/baseline geometry for the device. The analysis below is summarized from Korde (2015b) and is included for completeness. In the simulations discussed in

FIGURE 6

(a) Dashed line is the total exciting force; solid line is the relative exciting force. Relative exciting force larger than total exciting force leads to total movement less than relative movement. (b) Dashed line is the total exciting force; solid line is the relative exciting force. Two-spheres design provides large exciting force for the reaction frame. Peak of solid line means the largest difference between relative and total exciting forces at low frequency. (c) Hemispheres design for reaction frame provides the highest average difference between relative and total exciting forces, through peak difference value that is less than the spheres design.

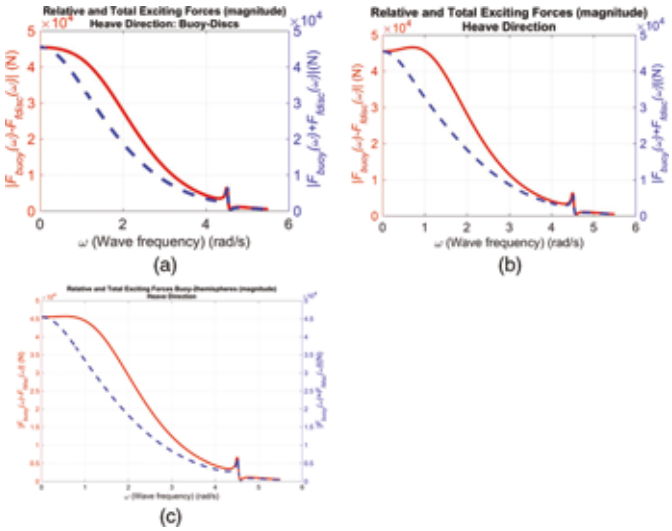

FIGURE 7

Effective radiation damping calculated without motion constraint. (a) Reaction frame with a flat top surface shows a second peak at low frequency. (b) Reaction frame with a deeper submerged design shows a lower value in radiation damping than that with the original design. (c) Larger design of reaction frame gives a higher value of effective radiation damping; flat top surface of reaction frame gives a high second peak value at low frequency.

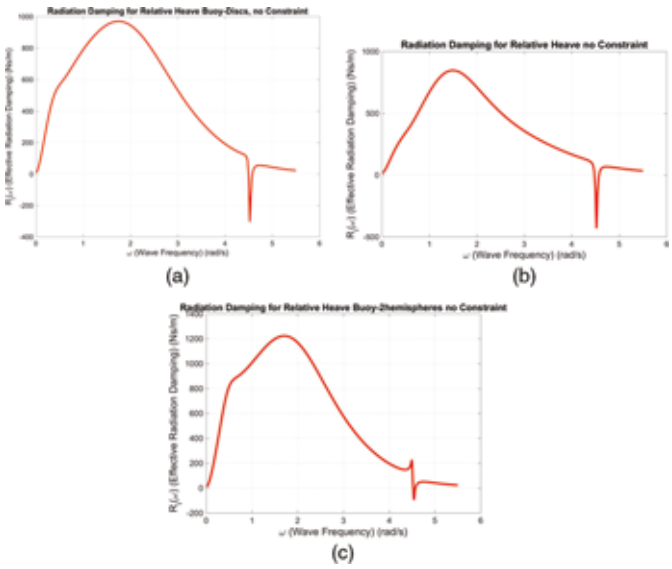

FIGURE 8

Calculation based on yearly data from MVCO (2017); constraint $\alpha_r = 1$ is applied to maintain feasible relative displacement range. Dashed line is buoy discs; solid line is buoy spheres. Best wave climate data of each month are collected to run this calculation. The two-spheres design of reaction frame shows slightly smaller control force.

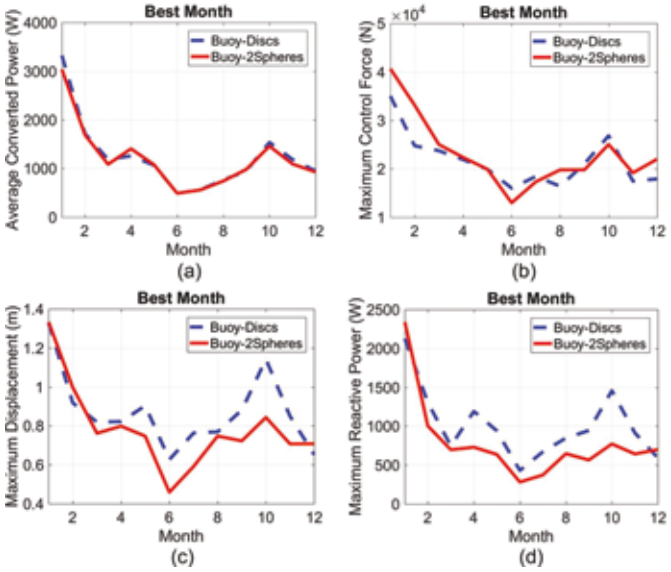

FIGURE 9

Calculation based on yearly data from MVCO (2017); constraint $\alpha_r = 1$ is applied to maintain feasible relative displacement range. Dashed line is buoy discs; solid line is buoy hemispheres. Best wave climate data of each month are collected to run this calculation. The two-hemispheres design of reaction frame shows greater energy conversion; meanwhile, control force increased significantly. Simulation results ~~of~~ buoy-discs design are consistent with those in Figure 12.

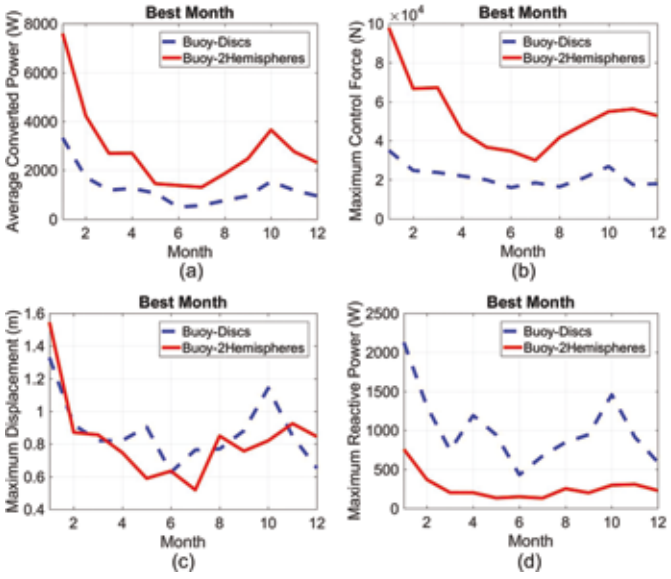

this work, radius of the cylinder portion of the buoy $R = 1.2$ m, and the draft $D_r = 1$ m. The instrument frame is 3 m below the water surface. For dynamic modeling purposes, it is found helpful to work in the frequency domain at first and then to use inverse Fourier transformation of the quantities of interest at the end. Thus,

$$\begin{aligned} &[Z_t(i\omega) + Z_L(i\omega)]v_t(i\omega) + i\omega[Z_c(i\omega) - Z_L(i\omega)]v_b(i\omega) = F_{ft}(i\omega) \\ &[Z_c(i\omega) - Z_L(i\omega)]v_t(i\omega) + [Z_b(i\omega) + Z_L(i\omega)]v_b(i\omega) = F_{fb}(i\omega) \end{aligned} \tag{9}$$

,where the matrix elements are defined as

$$\begin{aligned} Z_t(i\omega) &= i\omega[m_t + \bar{a}_t(\infty) + a_t(\omega)] + \frac{k_t}{i\omega} + (c_{dt} + b_{dt}(\omega)) \\ Z_b(i\omega) &= i\omega[m_b + \bar{a}_b(\infty) + a_b(\omega)] + \frac{k_b}{i\omega} + (c_{db} + b_{db}(\omega)) \\ Z_c(i\omega) &= i\omega\, a_c(\omega) + b_c(\omega) \\ Z_L(i\omega) &= L(\omega) + \frac{N(\omega)}{i\omega} \end{aligned} \tag{10}$$

where the letter m is used to denote in-air mass, with the subscripts t and b, respectively, denoting the top and bottom bodies. b_{dt} and b_{db} denote the frequency-variable radiation damping for the two bodies, while $\bar{a}_t(\infty)$ and $\bar{a}_b(\infty)$ denote the infinite-frequency added masses for the two bodies and $a_t(\omega)$ and $a_b(\omega)$ represent only the frequency-dependent parts of the respective added masses. The letter k denotes stiffness (hydrostatic for the floating buoy and mooring-related for the submerged body), while c_{dt} and c_{db} represent the linearized viscous damping coefficients. a_c and b_c denote the frequency-variable added mass and radiation damping due to interaction between the two bodies. Z_L represents the load impedance applied by the power takeoff on the relative oscillation. Following the approach of Falnes (1998), it is possible to express equation (9) as a scalar equation in terms of the relative velocity $v_r(i\omega)$,

$$v_r(i\omega) = v_t(i\omega) - v_b(i\omega) \tag{11}$$

by defining,

$$\bar{Z}(i\omega) = Z_t(i\omega) + Z_b(i\omega) + 2Z_c(i\omega) \tag{12}$$

and

$$F_e(i\omega) = \frac{F_{ft}(i\omega)(Z_b(i\omega) + Z_c(i\omega))}{\bar{Z}(i\omega)} - \frac{F_{fb}(i\omega)(Z_t(i\omega) + Z_c(i\omega))}{\bar{Z}(i\omega)} \tag{13}$$

It is seen that

$$v_r(i\omega) = \frac{F_e(i\omega)}{Z_i(i\omega) + Z_L(i\omega)} \tag{14}$$

where

$$Z_i(i\omega) = \frac{Z(i\omega)Z_s(i\omega) - Z_c^2(i\omega)}{\bar{Z}(i\omega)} \tag{15}$$

Details of the subsequent steps are provided in Korde (2015a). Following Falnes (1998) and Korde (2015a), the relative velocity is found to be at the hydrodynamic optimum (i.e., providing the best power conversion) when

$$Z_{Lnu}(i\omega) = Z_{ni}^*(i\omega) \tag{16}$$

which leads to

$$v_{ro}(i\omega) = \frac{F_e(i\omega)}{2\,R_i(\omega)} \tag{17}$$

where

$$Z_{ni}(i\omega) = R_i(\omega) + i\,C_i(\omega) \tag{18}$$

$R_i(i\omega)$ and $C_i(i\omega)$ are the resistive and reactive parts, respectively, of the effective impedance experienced by the relative velocity $v_r(i\omega)$. This can be verified by following the steps in Korde (2015a). Oscillation constraints are applied by following the approach of Evans (1981) on the relative v_r. In particular, R_i in equation (18) is replaced by $R_i(\omega) + \Lambda_r(\omega)$ where

$$\Lambda_r(\omega) = \frac{|F_e(i\omega)|}{2\beta_r(\omega)} - R_i(\omega) \tag{19}$$

where $\beta_r(\omega)$ represents the velocity constraint expressed as $\beta_r(\omega) = |i\omega\alpha_r|$. α_r is the maximum displacement allowed by the swept volume constraint on the buoy oscillation and actuator length when fully retracted. It should be noted that the constraint as specified in the frequency domain may not be satisfied in the time domain in some wave conditions. Constraint satisfaction therefore needs to be verified after each simulation run.

$Z_{ni}(i\omega)$ is then amended as

$$Z_{ni}(i\omega) = R_i(\omega) + \Lambda_r(\omega) + iC_i(\omega) \tag{20}$$

The exciting forces in heave for the two bodies can be expressed in frequency domain as

$$\begin{aligned} F_{ft}(i\omega) &= H_{ft}(i\omega)\,\eta(x_B;\, i\omega) \\ F_{fb}(i\omega) &= H_{fb}(i\omega)\,\eta(x_B;\, i\omega) \end{aligned} \tag{21}$$

$H_{ft}(i\omega)$ and $H_{fb}(i\omega)$ are the exciting force frequency response functions for the individual bodies (evaluated for unit incident wave amplitudes at their respective centroids); $\eta(x_B; i\omega)$ denotes the incident free-surface elevation at the body centroid x_B. The effective heave force (acting on the relative oscillation v_r [Falnes, 1998]) $F_e(i\omega)$ can then be expressed as

$$F_e(i\omega) = H_e(i\omega)\,\eta(x_B; i\omega) \tag{22}$$

The hydrodynamically optimum velocity can then be expressed as

$$v_{ro}(i\omega) = \frac{H_e(i\omega)}{2[R_i(\omega) + \Lambda_r(\omega)]}\ \eta(x_B;\ i\omega) \tag{23}$$

Taking the inverse Fourier transform of equation (23),

$$v_{ro}(t) = \int_{-\infty}^{\infty} h_o(\tau)\,\eta(x_B;\ t-\tau)\mathrm{d}\tau \tag{24}$$

where

$$h_o(t) = \frac{1}{2\pi}\int_{-\infty}^{\infty} \frac{H_e(i\omega)}{(2[R_i(\omega) + \Lambda_r(\omega)])}\, e^{i\omega t}\mathrm{d}\omega \tag{25}$$

$h_o(t)$ is noncausal for the two-body device in Figure 4. However, for $t < 0$, $h_o(t)$ can be truncated as $t \rightarrow -t_T$, where in the present case, $t_T \approx 30$ s, implying that $\eta(x_B; t)$ needs to be known at least 30 s ahead. With $\eta(x_B; t)$ predicted as summarized in Deterministic Wave Prediction, the resistive and reactive control forces can be determined as

$$\begin{aligned} F_l(t) &= \int_{-\infty}^{\infty} h_{ri}(\tau)\,\eta(x_B; t-\tau)\mathrm{d}\tau \\ F_a(t) &= \int_{-\infty}^{\infty} h_{ci}(\tau)\,\eta(x_B; t-\tau)\mathrm{d}\tau \end{aligned} \tag{26}$$

where

$$\begin{aligned} h_{ri}(t) &= \frac{1}{2\pi}\int_{-\infty}^{\infty} \frac{H_e\ i\omega}{2}\ e^{i\omega\ t}\ \mathrm{d}\omega \\ h_{ci}(t) &= \frac{1}{2\pi}\int_{-\infty}^{\infty} \frac{(H_e(i\omega)C_i(\omega))}{([2R_i(\omega) + \Lambda_r(\omega)])}\ e^{i\omega t}\mathrm{d}\omega \end{aligned} \tag{27}$$

To find the forces in the presence of oscillation constraints, $R_i(\omega)$ above is replaced by $R_i(\omega) + \Lambda(\omega)$. (Note that these integrals in the present work are evaluated from $-t_T$ to the present time t and $\eta(x_B; t)$ is predicted t_T beyond the present time t.)

With and without the oscillation constraint present, the average power absorbed over a period $[0, T]$ can be found using

$$P_w = \frac{1}{T}\int_0^T F_l(t)v_{ro}(t)\ \mathrm{d}t \tag{28}$$

Calculations

The calculations were focused on a specific application where the requirement is to provide a constant power amount (on the order of tens of watts) to a science instrument currently operating off Martha's Vineyard, Massachusetts, United States. The buoy was chosen to match the central surface mooring in the Pioneer Array of the Ocean Observatories Initiative (OOI Pioneer Array, 2017). The geometry optimization study of Geometry Optimization informed the design of the support framework for the instrument. Wave data collected by the 12-m node of the MVCO of the Woods Hole Oceanographic Institution were used to test the performance of the proposed designs in computer simulations (MVCO, 2017). Specifically, the complete yearlong wave data for 2015 were reviewed, and in order to obtain reasonable performance bounds, the best and the weakest wave conditions in terms of available wave energy were chosen for the simulations. The data are available in terms of significant wave heights and dominant periods for both swell and wind-wave components, leading to a bimodal wave spectrum overall. Waves were assumed to be largely long-crested for the site of deployment, although this assumption is not strictly necessary in view of other recent work (Korde et al., 2017). Simulations were carried out to map the performance of the system on two time scales. First, the most energy-rich and energy-poor significant wave heights—dominant period (swell and wind waves) combinations occurring in each month of 2015—were chosen to sample the seasonal variations of the available energy. Second, to sample the hourly variations of energy, the best day of the best month and the weakest day of the weakest month (in terms of energy availability) were also chosen for simulation. Using the two reported significant wave heights and two dominant periods (swells and wind seas) for each simulation test case, 10-min–long

irregular wave records were generated using a standard two-parameter bimodal spectral formulation as

$$S(\omega) = \sum_{i=1}^{2} \frac{(131.5H_{si}^2)}{T_{ei}^4 \omega^5} exp[-\frac{1054}{(T_{ei}\omega)^4}] \quad (29)$$

where the contributions of swell and wind seas are added together as shown in equation (29).The wave surface elevation at (x, t) can be expressed as

$$\eta(x;\ t) = \sum_{n=1}^{N} \Re\{(A(\omega_n)(exp[-i(k(\omega_n)x - \omega_n t + \vartheta_n)])\} \quad (30)$$

where

$$A(\omega_n) = \sqrt{(2S(\omega_n)\Delta\omega)} \quad (31)$$

and ϑ_n is a random phase angle between ϵ $[0, 2\pi]$, with $S(\omega_n)$ representing the spectral density value at ω_n. $N = 512$ was used in these calculations.

The buoy dimensions and the reaction frame dimensions for these time-domain simulations are shown in Figures 5(a)–5(c). Recall that it is the relative heave oscillation between the two bodies that is utilized for conversion and that the instrument is housed within the framework supporting the reaction mass. Relative oscillations need to be less than the total separation between the buoy and the reaction mass. To avoid iterative calculations and use of inequalities, the constraint is here specified in terms of the buoy draft (i.e., $\alpha_r = nD_r$, where $n = 1, 2, 3, \ldots$) so as to ensure that (i) the swept volume constraint is not exceeded and (ii) the greatest relative oscillation amplitude allowed by the constraint can be utilized for power conversion. Results discussed here include the captured power variation for the best wave conditions each month, weakest wave conditions each month, hourly wave conditions on the best day of the best month, and hourly wave conditions on the weakest day of the weakest month. As mentioned earlier, the complete year's data for 2015 were used to arrive at the chosen wave conditions. Finally, also included are results showing the maximum control force requirement in each case above and the maximum displacement noted (i.e., relative displacement between the buoy and the reaction frame) for each case simulated.

FIGURE 10

Calculation based on yearly data from MVCO (2017); constraint $\alpha_r = 2.5$ is applied to keep energy capture level. Dashed line is buoy discs; solid line is buoy spheres. Worst wave climate data of each month are collected to run this calculation. The two-spheres design of reaction frame shows a smaller maximum value of reactive power. ~~Contribute to easy energy storage design.~~

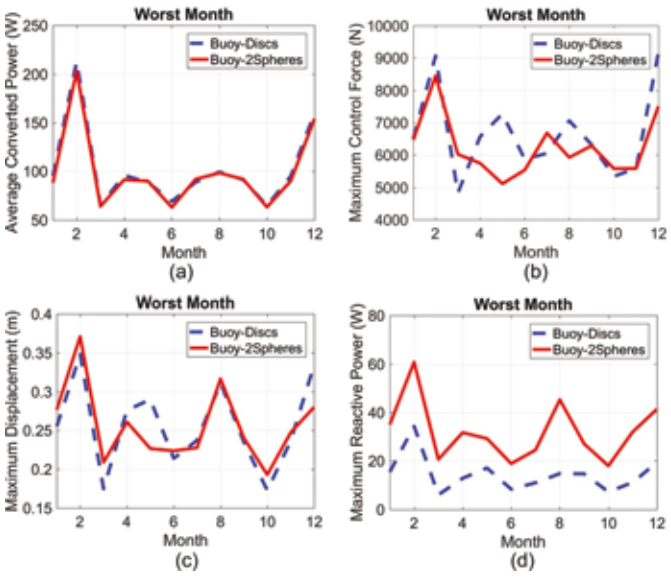

Discussion

As indicated in the Calculations section, the results discussed here span a range of wave conditions sampled from the wave data reported at the site of deployment. Figures 8–13 summarize the simulation results. Principal observations are highlighted below. Recall that these results examine the performance with wave-by-wave near-optimal control. The discussion below compares power capture performance of the three geometries for the reaction frame (see Geometry Optimization section). The two-disc reaction frame is referred to as the baseline geometry.

Figures 8 and 9 show that, as expected, best wave conditions vary over the year. In particular, in energy-rich

FIGURE 11

Calculation based on yearly data from MVCO (2017); constraint α_r = 2.5 is applied to maintain feasible relative displacement range. Dashed line is buoy discs; solid line is buoy hemispheres. Worst wave climate data of each month are collected to run this calculation. The two-hemispheres design of reaction frame still shows greater energy conversion; control force with smaller constraint α_r shows a lower value compared with that of the original design. Simulation results of buoy-discs design are consistent with those in Figure 8.

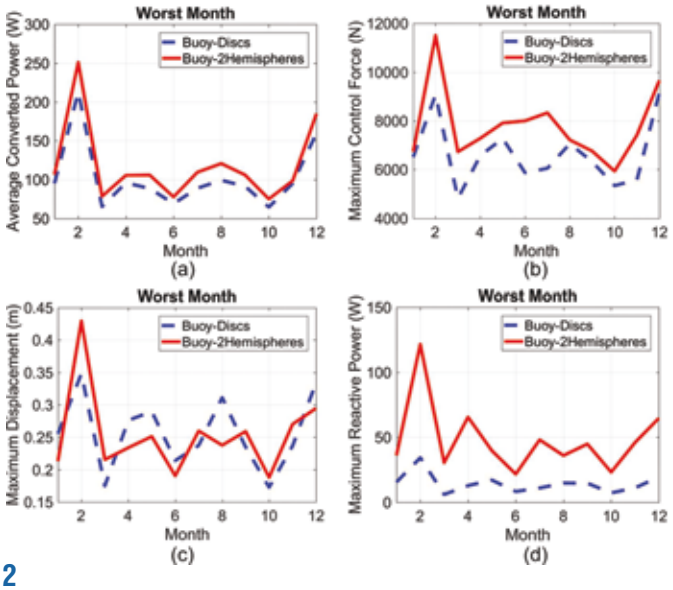

FIGURE 12

Part (a) shows converted power by buoy-discs design, buoy-spheres design, and buoy-hemispheres design constraint α_r = 2.5. Dashed line is buoy discs, solid line is buoy spheres, and dash-dot line is buoy hemispheres. This figure uses significant wave height H_s = 0.2 m.

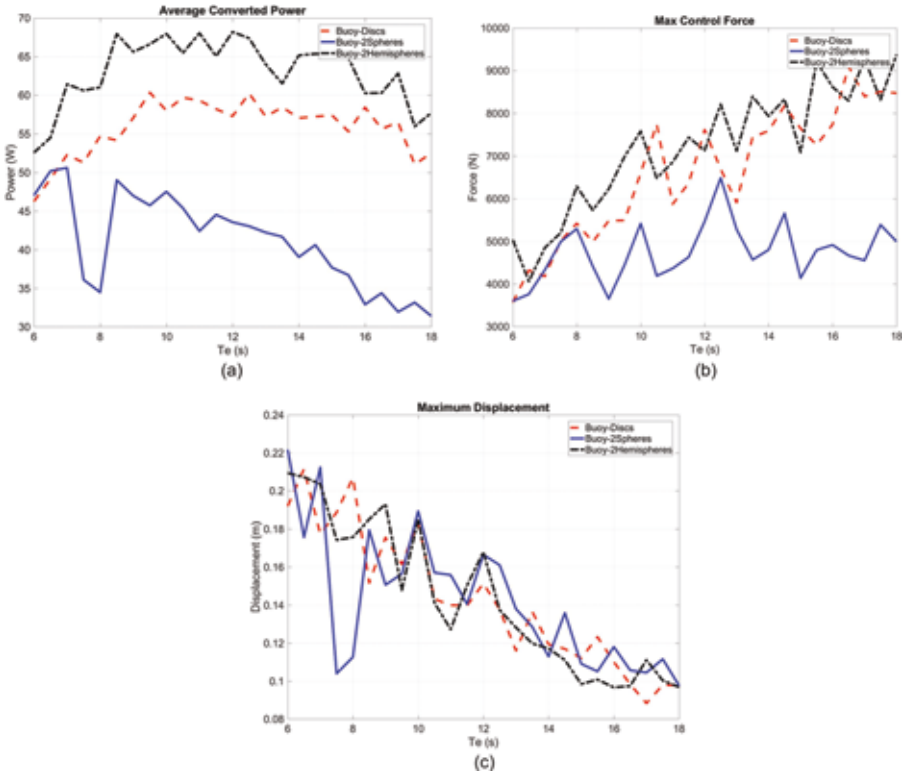

wave conditions, the significant wave heights can sometimes exceed 3 m, while in weaker wave conditions, significant wave heights can be on the order of 0.2 m. Therefore, the system hardware needs to be designed for a wide range of operating conditions to enable power conversion in the largest as well as smallest waves. In favorable wave conditions, 10-min averages for converted power show that over 7-kW average power can be converted by allowing the maximum relative displacement between the bodies to exceed 1.5 m. Note that the maximum control forces (shown in Figures 8(b) and 9(b)) are just the parts of the control force that require wave prediction (which includes the resistive load for power conversion and the reactive load for canceling the effect of the frequency-variable added masses of the two bodies). The part not requiring prediction is the reactive force required to cancel the contributions of the rest masses and the infinite-frequency added masses of the two bodies and the hydrostatic stiffness of the buoy. The total maximum control forces can exceed 300 kN in the very large waves. Figures 8(a) and 9(a) show that, even in the months with overall weaker wave climates, close to 500 W can be converted during parts of a day.

Figures 10 and 11 for the least favorable wave conditions show that the 10-min average power conversion enabled by the wave-by-wave near-optimal control can at times drop to less than 70 W (10-min average). The relative displacement amplitudes and control force magnitudes are also considerably smaller. Therefore, the control system enabling near-optimal performance appears necessary in periods of low wave activity at the present site. Furthermore, given the

FIGURE 13

This figure shows converted power result (15a) from H_{s1} = 0.3 m, H_{s2} = 0.2 m, and constraint α_r = 2.5; buoy-hemispheres design has higher converted power over T_{e1} and T_{e2} spacing.

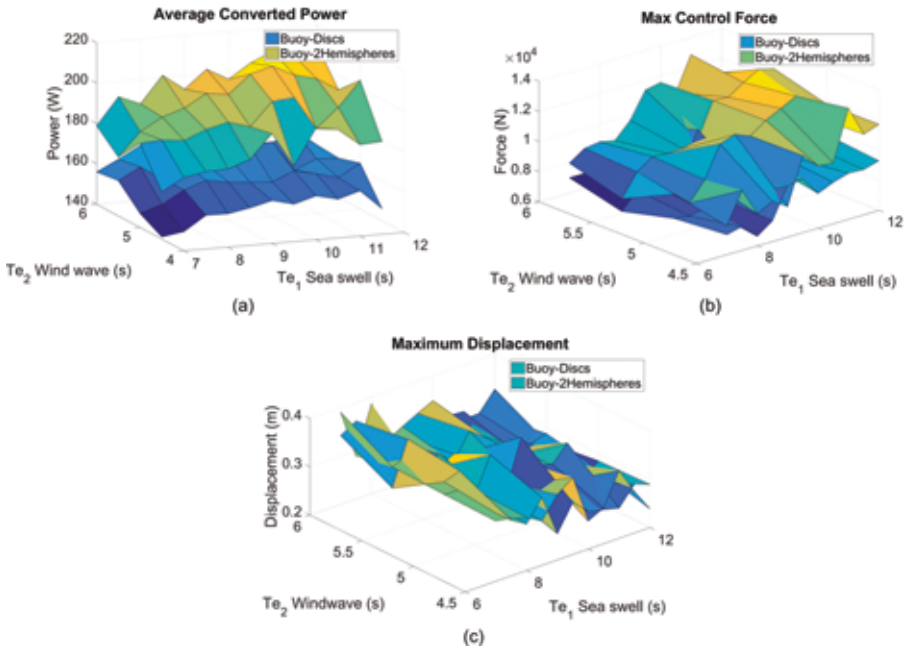

large variance between the best and worst wave conditions, the actuator/power takeoff also needs to be capable of operating efficiently over a wide range of force, stroke, and power requirements.

The sets of Figures 8 and 9 compare performance with three geometries. It is found that the reaction mass with two hemispheres provides the best performance overall in terms of greater capture but in general also requires a greater noncausal control force. On the other hand, the two-sphere reaction mass provides comparable or slightly less efficient power capture performance but requires a smaller noncausal control force. Given the small size of the bodies, wave diffraction effects are small, and the Froude-Krylov force component (due to incident wave potential alone) dominates. It can intuitively be seen that the net downward component of the Froude-Krylov force is greater for the two-hemisphere design (relative to the two-disc body), thus providing better force compensation and leading to greater effective radiation damping, which enables greater power conversion from the relative oscillation at impedance matching under oscillation constraints. The noncausal control force requirement is greater because the frequency-variable added mass is also greater. The opposite is true for the two-sphere geometry, which is effectively situated lower than the two-hemisphere geometry. The magnitude of the Froude-Krylov force acting on the two-sphere body is thus somewhat smaller. In addition, the symmetry of the spheres provides no advantage relative to the two-disc body in terms of the downward Froude-Krylov force. It is important, however, to compare the complete control forces (causal + noncausal) for a comparison with more immediate design relevance.

Conclusions

Buoys and moorings supporting ocean sensing instrumentation typically use solar, wind, or battery power, despite the ready availability of a denser, more predictable energy source in the form of ocean surface waves. This is understandable because current wave energy conversion technology is unable to meet the continuous power availability requirements of instruments through changing seasons unless the converters used are large enough. Often, this size requirement makes wave energy conversion technology incompatible with buoy sizes common to oceanographic applications. The work discussed above investigated enhancements that may enable integration of wave power conversion hardware into "small" oceanographic buoys (with a 1.2-m radius). The focus was on utilizing a two-body axisymmetric system where the top body is the oceanographic buoy and the lower body is a framework that houses a science instrument.

It was found that, with near-optimal wave-by-wave control, average power conversion ranged from 7 kW to 70 W in the best and weakest wave conditions reported near the site of instrument deployment. This control approach required bidirectional energy exchange between the converter and the power takeoff (here, a hydraulic cylinder). To make this possible, short-term (on the scale of wave periods) energy storage was required, which was enabled by a hydraulic accumulator. Another observation that followed from the results so far was that the total energy converted from waves over the year 2015 significantly exceeded the total energy consumed by the instrument over the same period. Consequently, waves at the present site of operation alone

would be sufficient as an energy source for instrument operation. However, because wave climate variability ranged from monthly to hourly time scales, it is evident that an energy storage system is required, so that a "guaranteed" constant power supply can be maintained for continuous instrument operation. An added advantage of an energy storage system is expected to be an ability to enhance the overall economics of the system by optimizing the use of the large excess power generated in highly favorable wave conditions. Work on this goal is currently underway and will be reported on separately. Furthermore, it is also important that the control, as proposed, be evaluated in experimental testing. Results on forthcoming tests will also be presented in a separate forum.

Acknowledgments

The authors are grateful to the U.S. National Science Foundation for supporting this research. This work is supported by the U.S. National Science Foundation under Grant 1702327. The views, opinions, and/or findings expressed are those of the authors and should not be interpreted as representing the official views or policies of the National Science Foundation or the U.S. Government. Particular thanks are due to Kandace Binkley and the Division of Ocean Sciences for their insights, interest, and support. The authors also thank Heidi Sosik, Don Peters, and Paul Matthias of the Woods Hole Oceanographic Institution for several helpful discussions.

Corresponding Author:

Umesh A. Korde
Department of Mechanical Engineering-Engineering Mechanics, Michigan Technological University, Houghton, MI 49931-1295
Email: uakorde@mtu.edu

References

Babarit, A., & Clement, A. H. 2006. Optimal latching control of a wave energy device in regular and irregular waves. Appl Ocean Res. 28(2):77-91. https://doi.org/10.1016/j.apor.2006.05.002.

Belmont, M. R., Horwood, J. M. K., Thurley, R. W. F., & Baker, J. 2006. Filters for linear sea-wave prediction. Ocean Eng. 33(17–18): 2332-51. https://doi.org/10.1016/j.oceaneng.2005.11.011.

Budal, K. 1985. Floating structure with heave motion reduced by force compensation. In: Proc. ASME Offshore Mechanics and Arctic Engineering Conference. 1:92-101. Dallas, TX.

Budal, K., & Falnes, J. 1977. Optimum operation of improved wave power converter. Mar Sci Commun. 3:133-50.

Budal, K., & Falnes, J. 1978. Wave power conversion by point absorbers. Norw Maritime Res. 6(4):2-11.

Budal, K., & Falnes, J. 1980. Interacting point absorbers with controlled motion. In: Power from Sea Waves, ed. Count, B., pp. 381-99. London, UK: Academic Press.

Count, B.M. 1978. On the hydrodynamic behavior of the OWC device. Proc Royal Soc Lond A. 363:559-78. https://doi.org/10.1098/rspa.1978.0183.

Evans, D. 1981. Power from water waves. Annu Rev Fluid Mech. 13:157-87. https://doi.org/10.1146/annurev.fl.13.010181.001105.

Evans, D., Jerey, D., Salter, S., & Taylor, J. 1979. Submerged cylinder wave energy device: Theory and experiment. Appl Ocean Res. 1(1):3-12. http://dx.doi.org/10.1016/0141-1187(79)90003-8.

Falcao, A. 2010. Wave energy utilization: A review of the technologies. Renew Sust Energ Rev. 14:899-918. https://doi.org/10.1016/j.rser.2009.11.003.

Falnes, J. 1995. On non-causal impulse response functions related to propagating water waves. Appl Ocean Res. 17(6):379-89. https://doi.org/10.1016/S0141-1187(96)00007-7.

Falnes, J. 1998. Wave-energy conversion through relative motion between two single-mode oscillating bodies. In: Proc. ASME Offshore Mechanics and Arctic Engineering Conference. Lisbon, Portugal.

Falnes, J., & Hals, J. 2012. Heaving buoys, point absorbers and arrays. Phil Trans Royal Society A. 370:246-77. https://doi.org/10.1098/rsta.2011.0249.

Falnes, J., & Kurniawan, A. 2015. Fundamental formulae for wave-energy conversion. Roy Soc Open Sci. 2(3):140305. http://dx.doi.org/10.1098/rsos.140305.

Hals, J. 2013. Practical limits to the power that can be captured from ocean waves by oscillating bodies. Int J Mar Energ. 3-4: e70e81. https://doi.org/10.1016/j.ijome.2013.11.012.

Hansen, R., & Kramer, M. 2011. Modeling and control of the wave star prototype. In: Proc. 9th European Wave and Tidal Energy Conference, Paper 163. Southampton, UK.

Hoskin, R.E., Count, B.M., Nichols, N., & Nicol, D.A.C. 1985. Phase control for the oscillating water column. In: Proc. IUTAM Symp. Hydrodynamics of Wave Energy Utilization, eds. Evans, D.V., & Falcao, A.F.O., pp. 257-68. Berlin, Germany: Springer Verlag.

Korde, U.A. 2015a. Near-optimal control of a wave energy device in irregular waves with deterministic-model driven incident wave prediction. Appl Ocean Res. 53:31-45. https://doi.org/10.1016/j.apor.2015.07.007.

Korde, U.A. 2015b. Performance of two 2-body heaving axisymmetric wave energy converters under control in irregular waves. In: Proc. 11th European Wave and Tidal Energy Conference (EWTEC). Nantes, France.

Korde, U.A., Robinett, R.D., Wilson, D.G., Bacelli, G., & Abdelkhalik, O.O. 2017. Wave-by-wave control of a wave energy converter with deterministic wave prediction. In: Proc.

European Wave and Tidal Energy Conference (EWTEC), Cork, Ireland.

McCormick, M. 2010. Ocean Engineering Mechanics: With Applications. Cambridge, UK: Cambridge University Press.

MVCO. 2017. Martha's Vineyard Coastal Observatory. Available from www.whoi.edu/mvco. (accessed October 2016).

Naito, S., & Nakamura, S. 1985. Wave energy absorption in irregular waves by feed-forward control system. In: Proc. IUTAM Symp. Hydrodynamics of Wave Energy Utilization, eds. Evans, D., & de O. Falcao, A., pp. 269-80. Berlin, Germany: Springer Verlag.

Nebel, P. 1992. Maximizing the efficiency of wave-energy plants using complex conjugate control. P I Mech Eng I-J Sys. 206(4):225-36. https://doi.org/10.1243/PIME_PROC_1992_206_338_02.

Newman, J. 1978. Marine Hydrodynamics. Cambridge, MA: MIT Press.

Ocean Observatories Initiative. 2017. Ocean Observatories Initiative. Available from http://oceanobservatories.org/technical-data-package/ (accessed January 2017).

OOI Pioneer Array. 2017. Available from https://ooinet.oceanobservatories.org/.

Ringwood, J.V., Bacelli, G., & Fusco, F. 2014. Energy-maximizing control of wave-energy converters. IEEE Contr Syst Mag. 34(5): 30-55. https://doi.org/10.1109/MCS.2014.2333253.

Salter, S. 1978. Development of the duck concept. In: Proc. Wave Energy Conference. Heathrow, U.K.

Schetzen, M. 1980. The Volterra and Wiener Theories of Nonlinear Systems. New York, NY: John Wiley & Sons.

WAMIT. 2012. WAMIT 7.0 User Manual. MIT, Cambridge, MA: The Massachusetts Institute of Technology.